Front. Mater. Sci. 2024, 18(3): 240696
https://doi.org/10.1007/s11706-024-0696-6

RESEARCH ARTICLE

# Femtosecond laser-induced graphene for temperature and ultrasensitive flexible strain sensing

Mingle Guan[1,2], Zheng Zhang[1], Weihua Zhu[1], Yuhang Gao[1,2], Sumei Wang (✉)[1,2], and Xin Li[1]

1 Laser Micro/Nano Fabrication Laboratory, School of Mechanical Engineering, Beijing Institute of Technology, Beijing 100081, China
2 Yangtze Delta Region Academy of Beijing Institute of Technology, Jiaxing 314000, China



**ABSTRACT: Flexible sensors with high sensitivity and stability are essential components of electronic skin, applicable to detecting human movement, monitoring physiological health, preventing diseases, and other domains. In this study, we utilized a straightforward and efficient femtosecond laser direct writing technique using phenolic resin (PR) as a carbon precursor to produce high-quality laser-induced graphene (LIG) characterized by high crystallinity and low defect density. The fabricated LIG underwent comprehensive characterization using SEM, Raman spectroscopy, XPS, and XRD. Subsequently, we developed strain sensors with a hexagonal honeycomb pattern and temperature sensors with a line pattern based on PR-derived LIG. The strain sensor exhibited an outstanding measurement factor of 4.16 × $10^4$ with a rapid response time of 32 ms, which is applied to detect various movements like finger movements and human pulse. Meanwhile, the temperature sensor demonstrated a sensitivity of 1.49%/°C with a linear response range of 20–50 °C. The PR-derived LIG shows promising potential for applications in human physiological health monitoring and other advanced wearable technologies.**

**KEYWORDS: femtosecond laser; laser-induced graphene; flexible sensor; high sensitivity**

## Contents



Received May 22, 2024; accepted July 24, 2024

E-mail: wangsumei@bit.edu.cn

## 1 Introduction

Monitoring human physiological signals in real time is crucial for health surveillance and disease prevention. The emergence of electronic skin presents a promising way to achieve this objective. Generally, electronic skin utilizes a

flexible substrate that can be applied to human skin to monitor various physiological signals like pulse [1–2], body temperature [3–4], and movement [5–7], accurately and reliably. A crucial component of electronic skin is the high-performance flexible sensor, which must possess high sensitivity, stability, and flexibility [8–9]. Various materials, including metal nanomaterials [10–11], graphene [12–13], carbon nanotubes (CNTs) [14], and conductive polymers [15–16], have been developed for the manufacture of flexible sensors. Graphene, with its unique physical and chemical properties, holds immense promise for flexible sensing applications. Nevertheless, traditional methods like chemical vapor deposition (CVD) or mechanical stripping have disadvantages like complex processes, low manufacturing efficiency, and the utilization of toxic chemicals. In 2014, Tour's team discovered that polyimide (PI) could be transformed into three-dimensional (3D) porous graphene using $CO_2$ lasers. This breakthrough introduced laser-induced graphene (LIG) technology, offering a more flexible, efficient, and environmentally friendly approach to graphene production [17].

Laser direct writing technology offers advantages such as mask-free and programmable patterning. In recent years, extensive research has been conducted on LIG and its associated sensing applications, including strain sensing [18] and electrochemical sensing [19–20]. Li et al. [21] achieved a remarkable breakthrough based on the irradiation of a glucose/graphene/polydimethylsiloxane (PDMS) prepolymer film with an infrared (IR) laser, resulting in a novel skin-like flexible piezoresistive sensor with an ultra-high sensitivity of 1348 $kPa^{-1}$ at 0–2 kPa. Thakur et al. [22] introduced a manganese carbonate modified LIG ($MnCO_3$/LIG) composite electrode material for electrochemical glucose detection, showing a sensitivity of 2731.2 $\mu A \cdot mmol^{-1} \cdot L \cdot cm^{-2}$, which surpasses that of most $MnCO_3$-based composites. Furthermore, researchers have started to explore multi-functional sensors capable of measuring multiple parameters. Liu et al. [23] developed a degradable flexible sensor by transferring LIG onto a starch film. This sensor, featuring three modes for detecting strain, temperature, and pressure, represents a significant advancement in sensor technology. Currently, these multi-functional sensors encounter several challenges, such as a complex preparation process or low sensitivity. With an ultrashort pulse duration and extremely high peak intensity, the interactions of femtosecond lasers with materials are fundamentally different from those of long-pulse and continuous lasers. Femtosecond lasers are already employed to fabricate LIG flexible sensors. Le et al. [24] employed femtosecond laser pulses to construct a flexible temperature sensor on a leaf. After laser treatment, the leaf retains its original flexibility without any discernible damage. This temperature sensor offers a temperature coefficient of resistance (TCR) of −0.08%/°C. Using femtosecond laser temporal shaping and plasma ejection confinement, Hong et al. [25] developed a strain sensing unit with a resolution of 6.5 μm, achieving the current minimum line width of LIG. Femtosecond LIG offers a distinctive advantage in multi-sensor integration due to reduced thermal damage and enhanced resolution. Bai et al. [26] designed a temperature and pressure sensor array through femtosecond laser treatment and CNT coating, showing a resistance temperature coefficient of −0.52%/°C and a pressure sensor sensitivity of −2.01 $kPa^{-1}$. Zhu et al. [27] proposed a method for precisely reducing graphene oxide/gold composites using a shaping femtosecond laser, leading to the creation of strain and humidity sensors. The strain sensor exhibits a strain gauge factor (GF) of 67.2 within the strain range of 28.2%, while the sensitivity of the humidity sensor is increased by 68.4%.

In this investigation, phenolic resin (PR) served as the carbon precursor for femtosecond LIG. The graphitization process of PR was comprehensively investigated through conductivity testing, Raman spectroscopy, scanning electron microscopy (SEM), and X-ray photoelectron spectroscopy (XPS). Hexagonal cellular and linear structures were painstakingly fabricated and subsequently transferred onto a medical polyurethane (PU) film for strain and temperature detection, respectively. The sensor demonstrated a remarkable maximum strain GF of $4.16 \times 10^4$ and a TCR of 1.49%/°C, along with outstanding stability.

## 2 Experimental

### 2.1 Preparation of PR film

Ethanol-soluble PR powder was produced by Henan Borun Casting Material Co., Ltd. First, 4 g of PR powder was added to 10 mL of ethanol. After undergoing ultrasonic treatment at room temperature for 5 min, the mixture was left to stand for 24 h, generating a PR ethanol solution with a concentration of 400 $mg \cdot mL^{-1}$. Subsequently, a 2 cm × 2 cm cover glass was immersed in

an ethanol solution and subjected to ultrasonic cleaning for 10 min to guarantee a pristine substrate. Then, 200 mL of PR solution was poured into the center of the cover glass, and a two-step spin coating process was carried out: 150 r·min$^{-1}$ for 30 s, followed by 300 r·min$^{-1}$ for 70 s, resulting in formation of a PR film approximately 100 μm thick on the substrate. The PR film was cured through drying at 60 °C for at least 8 h.

The PR film is affixed onto the translation platform (Aerotech) and exposed to femtosecond laser irradiation (Yili, 1030 nm, 209 fs, 800 kHz). With an objective lens (10×, NA = 0.3, Olympus), the laser is focused onto the surface of the film. To facilitate real-time monitoring of the laser scanning process, an imaging setup consisting of a lamp, a charge-coupled device (CCD), and additional components is employed. The schematic illustration of the laser manufacturing system is presented in Fig. S1 (included by ESM of Appendix).

After the laser process, the film is immersed in ethanol for cleansing. Then, the graphitized area resulting from the laser treatment is removed, while the untreated part is dissolved in ethanol for reuse. The separated LIG pattern is subsequently transferred onto the medical PU film, with the LIG electrode connected to the copper wire by means of conductive tape. An extra layer of PU film is added to encase the sensing unit. The manufacturing diagram is sketched in Fig. 1(a). The strain sensing unit shows a hexagonal honeycomb structure and the temperature sensing unit shows a linear structure, with precise dimensions outlined in Fig. S2 (included by ESM of Appendix). The medical PU film displays superior transparency, exceptional air permeability, water resistance, and ease of application on the skin, as depicted in Fig. 1(b).

### 2.2 Characterization

The surface morphology of the LIG was studied through SEM using a high-resolution field emission scanning electron microscope (Hitachi S-4800, Japan) at an accelerating voltage of 10 kV. Raman spectra were acquired using a Raman spectrometer (Renishaw inVia-Qontor, Britain) by exciting the material with a 532 nm laser. XPS was performed on a PHI QUANTERA-II SXM instrument (Japan) with Al Kα radiation (1486.6 eV). The phase of the LIG surface structure was analyzed through X-ray diffraction (XRD) on a diffractometer (SmartLab SE, Japan). The tensile strain was applied with a universal testing machine (SHIMADZU AGS-X, Japan). A vacuum drying chamber (DZF-6034, China) was utilized for the heating and temperature sensor testing. A digital multimeter (Keysight 34465A, USA) was employed to measure the resistance.

## 3 Results and discussion

### 3.1 Analytical characterization

Firstly, the effect of the laser scanning speed on the surface morphology of the LIG was studied. The microscopic morphological differences of LIG under different scanning speeds at a laser fluence of 0.80 J·cm$^{-2}$ can be observed through SEM images (Fig. 2). When the scanning speed is 1000 μm·s$^{-1}$, the material shows a groove shape, as revealed in Figs. 2(a) and 2(d). At lower scanning speeds, excessive laser fluence is deposited at the same location, leading to strong removal of the material at the laser spot center. When the scanning speed is 2000 μm·s$^{-1}$, gas eruption during laser irradiation results in the formation of a porous structure, and a graphitic lamellar structure is formed around the hole, as shown in Figs. 2(b) and 2(e). At a scanning speed of 3000 μm·s$^{-1}$, the rapid scanning rate hinders the material from receiving sufficient energy, particularly in regions beyond the laser scanning path. Consequently, only a few

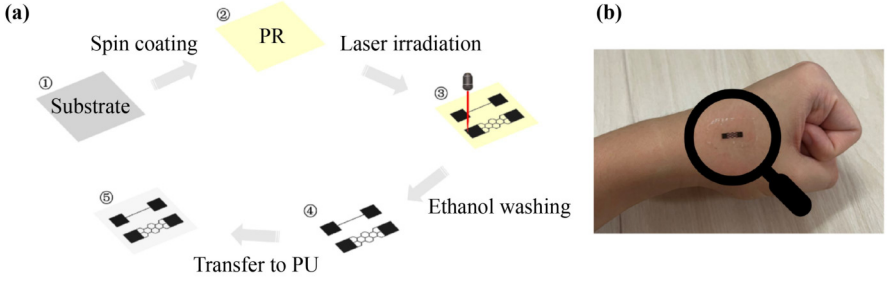


**Fig. 1** (**a**) Schematic illustration of the LIG sensor fabrication. (**b**) Schematic illustration of a medical PU film on the skin.

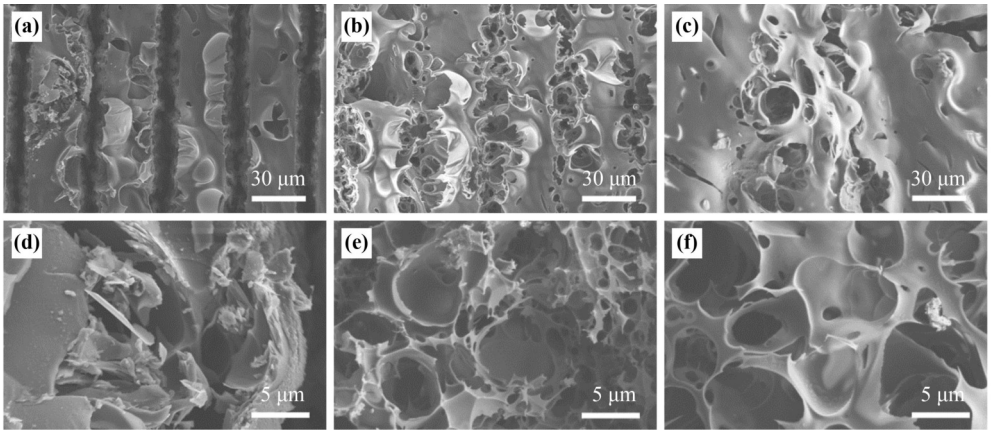


**Fig. 2** SEM images of LIG at a laser fluence of 0.80 J·cm$^{-2}$ with scanning speeds of (**a**)(**d**) 1000 μm·s$^{-1}$, (**b**)(**e**) 2000 μm·s$^{-1}$, and (**c**)(**f**) 3000 μm·s$^{-1}$.

holes appear on the material surface, as shown in Figs. 2(c) and 2(f).

The laser fluence also has a profound influence on the surface morphology of LIG. When the scanning speed is 3000 μm·s$^{-1}$, the microscopic morphologies of LIG under various laser fluences can be observed (Fig. 3). At a laser fluence of 0.80 J·cm$^{-2}$, the LIG surface exhibits a porous morphology with surface breaks due to the rapid release of gas products like $CO_2$, as seen in Figs. 3(a) and 3(b). Increasing the laser fluence to 1.13 J·cm$^{-2}$ leads to a higher energy density at the laser spot, resulting in removal of the material and creation of a trough structure on the existing porous morphology. This also results in the melting of the material around the laser spot, leading to the dispersion of fine carbon particles across the LIG surface, as depicted in Figs. 3(c) and 3(d). With a further increase in laser fluence to 1.95 J·cm$^{-2}$, significant thermal effects [28] occur in the surrounding areas of the laser spot, resulting in an increase in both size and number of carbon particles on the LIG surface, as shown in Figs. 3(e) and 3(f). Finally, at a fluence of 2.59 J·cm$^{-2}$, the porous structure is nearly eliminated, and the surface becomes covered with numerous fine particles formed due to material melting, as illustrated in Figs. 3(g) and 3(h).

We created a 2000 μm × 2000 μm square pattern and employed a digital multimeter with the dual probe method to measure and record resistance changes under varying laser fluences and scanning speeds, as depicted in Fig. 3(i). The resistance of graphene is affected by the combined effects of laser fluence and scanning speed. At lower fluence levels, resistance increases with higher scanning speeds. This occurs because as the scanning speed increases, the amount of laser energy received by the material per unit area becomes insufficient, resulting in reduced graphitization. On the contrary, at higher fluence levels, resistance decreases with increasing scanning speed. Lower scanning speeds lead to excessive energy deposition at the same position, causing structural damage in the graphene. To achieve low resistance, a low scanning speed is required at low fluence, while a high scanning speed is needed at high fluence. Therefore, the energy deposition rate per unit area significantly influences resistance. We calculate the energy deposition rate per unit area by dividing the laser fluence by the scanning speed. Through our calculations, it is observed that the energy deposition rate in the low resistance region (< 100 Ω) typically averages around 0.8.

Raman spectroscopy, XPS, and XRD were used to characterize LIG prepared by laser irradiation at various fluences. Figure 4 illustrates a comparison of the material characterization between LIG prepared under laser irradiation with a fluence of 2.59 J·cm$^{-2}$ at a scanning speed of 3000 μm·s$^{-1}$ and the original PR film. As depicted in Fig. 4(a), the Raman spectrum of LIG exhibits three distinct graphene characteristic peaks: the D peak at ~1350 cm$^{-1}$ (indicating disordered vibration and structural defects in graphene samples), the G peak at ~1580 cm$^{-1}$ (resulting from in-plane vibration of sp$^2$ carbon atoms), and the 2D peak at ~2700 cm$^{-1}$ (a second-order Raman peak attributed to two-phonon resonance linked to the number of graphene layers). The ratio of the D peak intensity to the G peak intensity ($I_D/I_G$ = 0.15) suggested a low defect density in LIG, and the ratio of the 2D peak intensity to the G peak intensity ($I_{2D}/I_G$ = 0.45) indicated a lower number of graphene layers [29]. Furthermore, the narrow full width at half maximum (FWHM) of the

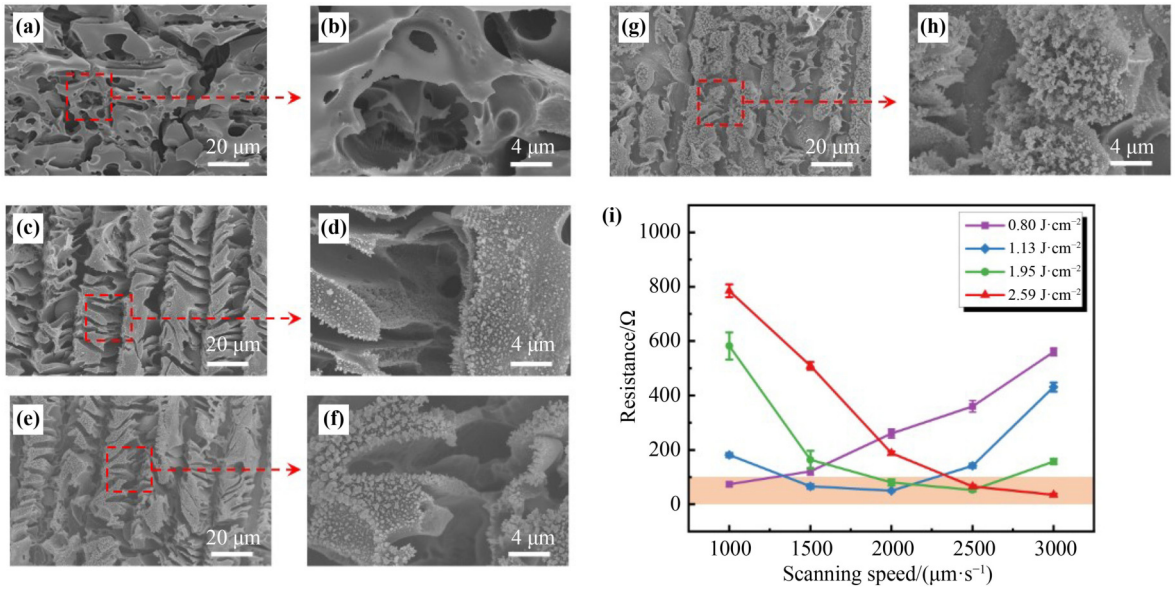


**Fig. 3** SEM images of LIG at a scanning speed of 3000 μm·s$^{-1}$ and laser fluences of (**a**)(**b**) 0.80 J·cm$^{-2}$, (**c**)(**d**) 1.13 J·cm$^{-2}$, (**e**)(**f**) 1.95 J·cm$^{-2}$, and (**g**)(**h**) 2.59 J·cm$^{-2}$. (**i**) Resistances of LIG towards different laser parameters.

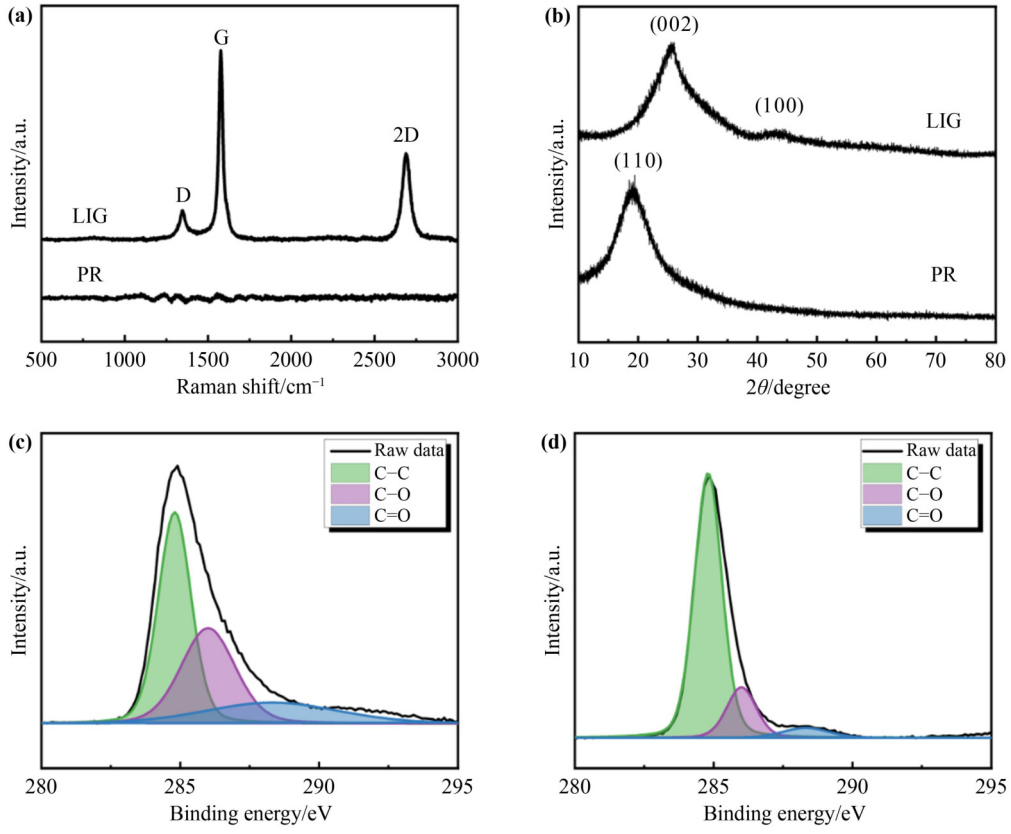


**Fig. 4** (**a**) Raman spectra of PR and LIG. (**b**) XRD patterns of PR and LIG. (**c**) High-resolution C 1s XPS spectrum of PR. (**d**) High-resolution C 1s XPS spectrum of LIG.

characteristic peak indicates a high level of crystallinity in LIG [30]. When the laser scanning speed is set at 3000 μm·s$^{-1}$ with an increase in laser fluence from 0.80 to 2.59 J·cm$^{-2}$, the Raman spectra in Fig. S3 (included by ESM of Appendix) depict a decrease in the intensity of the D peak and an increase in the 2D peak intensity. This

outcome signifies an improvement in carbonization quality. In Fig. 3(i), with the scanning speed fixed at 3000 μm·s$^{-1}$, an escalation in laser fluence results in a reduction in the resistance of the carbonization pattern and an elevation in conductivity, indirectly indicating an enhancement in carbonization quality. Thus, the analysis results from resistance measurement and Raman spectroscopy are congruent, suggesting that augmenting the laser fluence within a specific range can improve carbonization quality.

The graphitization transition of PR was further assessed using XRD. After laser irradiation, the XRD pattern exhibited a discernible peak near 26° (Fig. 4(b)), corresponding to the diffraction of the graphene (0 0 2) crystal face. High-resolution XPS was utilized to determine the chemical compositions of LIG, as shown in Fig. S4 (included by ESM of Appendix). With a laser scanning speed of 3000 μm·s$^{-1}$, an escalation in laser fluence resulted in an increase in the C content from ~67% to ~80%, while the O content decreased from ~33% to ~20%. Consequently, the C/O ratio gradually increased, indicating the removal of the oxygen element during laser treatment. Segmenting the high-resolution spectrum of the C 1s region revealed three peaks (Figs. 4(c) and 4(d)): C−C (284.8 eV), C−O (286.0 eV), and C=O (288.8 eV). The comparison of high-resolution spectra for the C 1s region at different laser fluences, as shown in Fig. S5 (included by ESM of Appendix), illustrates a decrease in C−O and an increase in C−C as the laser fluence rises. These observations confirm the graphitization transformation of PR under femtosecond laser irradiation.

### 3.2 Performance of LIG strain and temperature sensor

The LIG strain sensor is produced using a laser fluence of 2.59 J·cm$^{-2}$ and a scanning speed of 3000 μm·s$^{-1}$. The strain sensing unit features a hexagonal honeycomb structure. In contrast to the conventional single-wire structure, this design can efficaciously prevent the irreversible damage caused by the fracture of the sensor and enhance the bearable strain range of the sensor. Figures 5(a)–5(c) illustrate variations of the resistance with the tensile strain for the LIG sensor. As the material is stretched, it develops micro-cracks and undergoes a gradual separation between conductive structures, resulting in reduced electrical connectivity and consequently, an increase in resistance [31]. The GF value can be calculated using the following equation:

$$\mathrm{GF} = \frac{R - R_0}{R_0 \varepsilon} \tag{1}$$

where $R_0$ denotes the initial resistance of the sensor, and $R$ represents the resistance of the sensor under the strain $\varepsilon$. The strain response curve of the sensor demonstrates three distinct linear regions. In the low strain range (0–0.8%), the resistance gradually increases with a GF of 242, attributed to the initial development of micro-cracks. Within the moderate strain range (0.8%–2.8%), the resistance elevates more rapidly, displaying a GF of 1038, attributed to the expansion of micro-cracks and the occurrence of more cracks, the conductive path is randomly broken, resulting in a faster increase in resistance. At higher strain levels (2.8%–3.6%), the resistance sharply increases with a GF of 4.16 × 10$^4$. Another LIG strain sensor was fabricated using a laser fluence of 0.80 J·cm$^{-2}$ and a scanning speed of 3000 μm·s$^{-1}$. Its strain response, illustrated in Fig. S6 (included by ESM of Appendix), exhibits a GF of only 57.3, significantly lower than that of the strain sensor prepared under a laser fluence of 2.59 J·cm$^{-2}$. Hence, lower resistance and improved carbonization positively influence sensor sensitivity. Additionally, we speculate that the surface particles formed on LIG under high fluence laser also enhance sensitivity. These particles might contribute to quantum channel formation when graphene structures separate during stretching, resulting in significant resistance changes through the tunneling mechanism. This mechanism posits that when graphene structures are separated but remain close, electrons can traverse to form quantum tunnels. Resistance increases due to the tunneling effect varies significantly with the distance between adjacent graphene structures [32].

The sensor we designed shows a sharp increase in resistance up to 400 MΩ at 3.6% strain, while ensuring dependable electrical connections. During a 3.6% strain-recovery cycle lasting for 1 h, it consistently demonstrates a stable and reproducible response, as indicated in Fig. 5(d). Moreover, the sensor shows outstanding fast response capabilities, offering a rise time of 32 ms and a fall time of 20 ms, as depicted in Fig. 5(e).

The performance metrics of other strain sensors based on LIG from previous studies are outlined in Table 1 [33–41]. In contrast to existing literature, our sensor exhibits exceptional sensitivity.

The LIG sensor is also utilized for the detection of temperature. We crafted a linear design LIG temperature sensor using a 1.95 J·cm$^{-2}$ laser fluence and a scanning

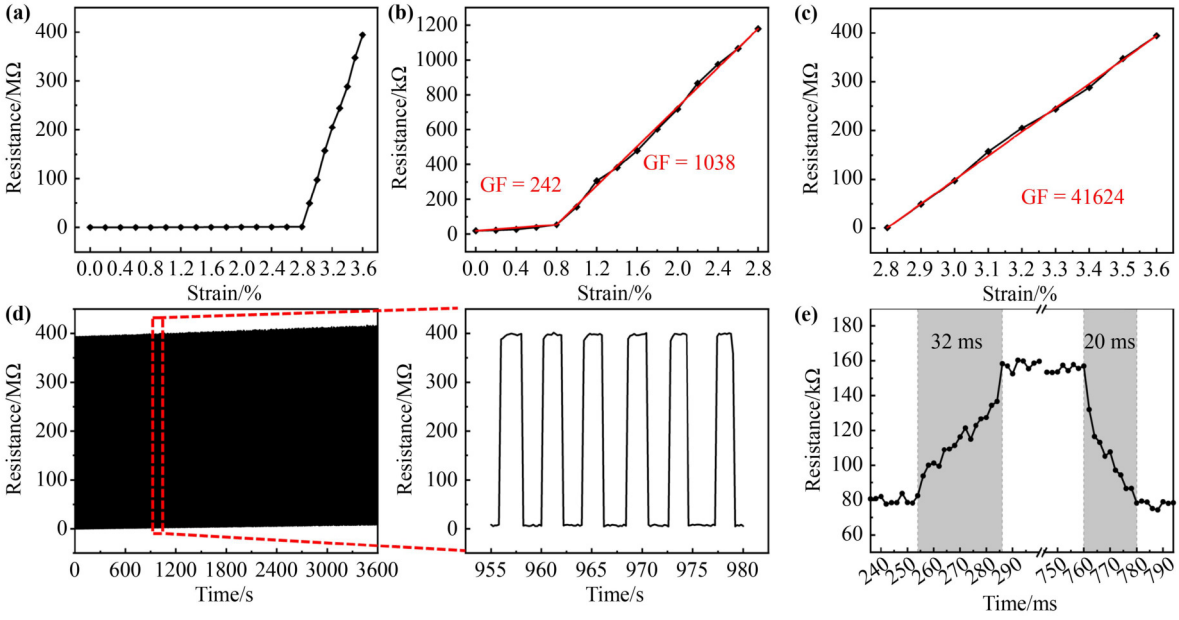


**Fig. 5** Strain sensing performances: (**a**) the resistance of the LIG strain sensor varies with tensile strain; (**b**) a magnified view of the change of the sensor's resistance in the strain range from 0 to 2.8%; (**c**) a magnified view of the change of the sensor's resistance in the strain range from 2.8% to 3.6%; (**d**) the sensor's response during a tensile release cycle test; (**e**) response time of the sensor.

**Table 1** Comparison of this LIG strain sensor and other graphene-based strain sensors reported in recent studies [33–41]

| Material | Pattern design | Strain/% | GF | Ref. |
|---|---|---|---|---|
| LIG (PR) | Hexagonal honeycomb | 0–0.8; 0.8–2.8; 2.8–3.6 | 242; 1038; 41624 | This work |
| $MoS_2$@LIG (PI) | Straight line | 0–16.7; 16.7–25 | 236.2; 1242 | [33] |
| LIG (PI) | Shutter pattern | 0–5; 5–9; 9–11 | 12.1; 61.5; 316.3 | [34] |
| LIG (PI) | Straight line | 0–10 | 456.51 | [35] |
| LIG (PEEK) | Corrugated structure | 0–1; 1–5; 5–6.8 | 150; 338.8; 2203.5 | [36] |
| Pt@LIG (PBI) | Straight line | 0–6; 6–16; 16–20 | 45.6; 269.5; 489.3 | [37] |
| LIG (PI fabric) | Straight line | 0–4 | 21.4 | [38] |
| Au&Cr + GNS | Interdigital structure | 0.15–0.2 | $6.38 \times 10^7$ | [39] |
| BP@LIG | Serpentine line | 0–7.5; 7.5–19.2; >19.2 | 81; 303; 2765 | [40] |
| LIG/PDMS | Straight line | 0–30; 30–50; 50–65 | 111.1; 624.5; 2212.5 | [41] |

Notes: BP, black phosphorus; GNS, graphene nanosheet; PBI, polybenzimidazole; PEEK, polyetheretherketone.

speed of 3000 μm·s$^{-1}$. The temperature sensing units featuring a linear pattern design can attain a high initial resistance and exhibit more pronounced resistance changes when influenced by temperature, which is conducive to accurately capturing the resistance variations caused by temperature alterations. Over a temperature range of 20–70 °C, resistance data from the LIG sensor were collected within 300 s at each temperature, as depicted in Fig. 6(a). Unlike the negative temperature coefficient reported in the literature for LIG, our LIG sensor exhibits an enhancement in resistance with the increase in temperature, indicating a positive temperature coefficient. During the sensor cleaning process, a small amount of PR dissolved in ethanol seeped into the porous structure of LIG. Upon drying, this dissolved PR solidified and filled the porous structure of LIG. As the temperature rose, the physical contact between LIG structures decreased, leading to an overall resistance increase due to the thermal expansion of PR. The TCR is calculated using the following equation to represent the temperature sensitivity of the sensor:

$$\mathrm{TCR} = \frac{R - R_0}{R_0 (T - T_0)} \tag{2}$$

where $R_0$ represents the initial resistance at the initial temperature $T_0$, and $R$ represents the resistance at the

corresponding temperature *T*. The resistance change curve of LIG at different temperatures is depicted in Fig. 6(b), revealing two main linear regions in its resistance change. When the temperature rises from 20 to 50 °C, the resistance changes, mainly driven by the thermal expansion of PR and PU film, is significantly influenced by temperature. We utilized the least square method for linear fitting of the resistance data, resulting in a TCR of 1.46%/°C. When the temperature rises from 50 to 70 °C, the structural separation caused by the expansion of PR gradually approaches saturation, leading to a TCR of 0.29%/°C.

### 3.3 Applications

Due to its remarkable sensitivity and flexibility, the LIG sensor enables the effective detection of subtle human movements. When activated, the movement of the finger bone propels the metacarpal bone, resulting in coordinated motion. Thus, monitoring the activity of the metacarpal bone indirectly provides information about finger movements. Affix the LIG sensor above the metacarpal bone linked to the index finger. Lift the index finger every 10 s and record the resistance response, as depicted in Fig. 7(a). Heart rate is a vital indicator of cardiovascular health, and its monitoring is crucial for preventing heart disease. Position the LIG sensor above the radial artery and record the resistance response within 10 s, as shown in Fig. 7(b). Calculations indicate that the subjects' heart rate was approximately 78 beats per minute in the relaxed state and about 112 beats per minute after exercise, which is within the normal range.

## 4 Conclusions

In summary, our research investigates the regulatory mechanism of femtosecond laser on the graphitization process of PR. We propose a straightforward and efficient femtosecond laser direct writing technique for producing

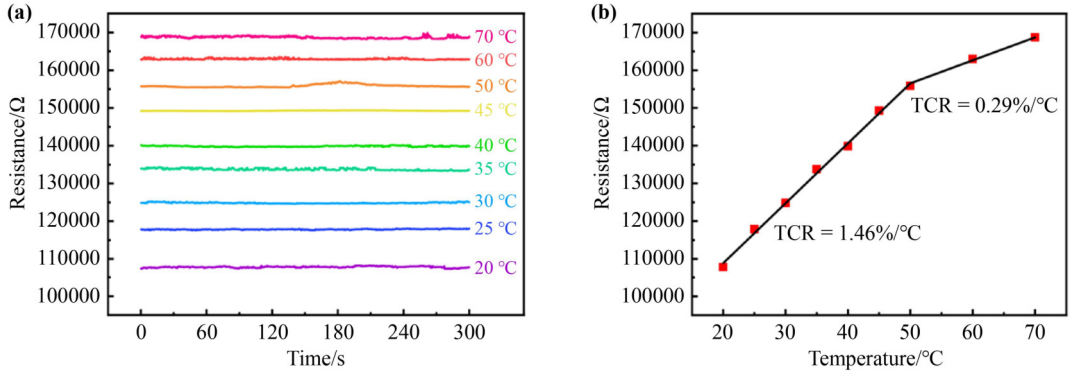


**Fig. 6** Temperature sensing performance: (**a**) stability response of the LIG sensor at 20–70 °C; (**b**) sensitivity of the LIG sensor.

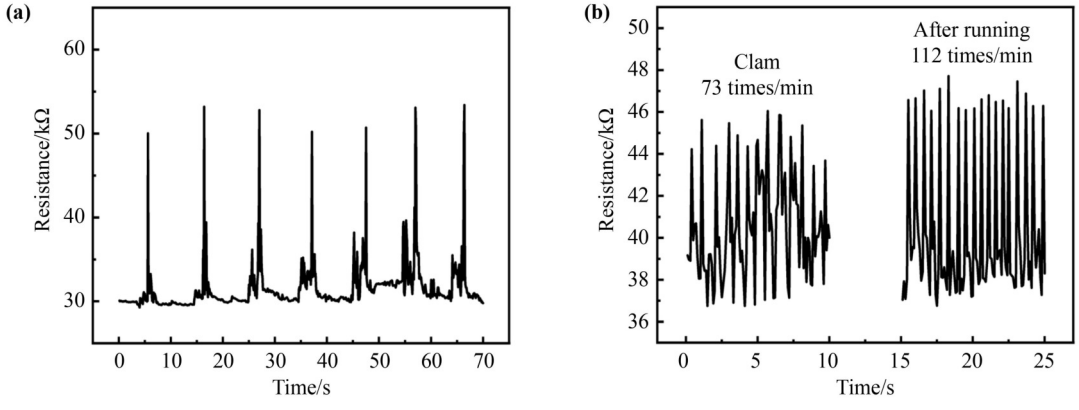


**Fig. 7** Real-time motion monitoring with the LIG sensor (the sensor was prepared with a 2.59 J·cm$^{-2}$ laser fluence and a scanning speed of 3000 μm·s$^{-1}$): (**a**) real-time resistance response of the sensor at the metacarpal bone during finger movement; (**b**) real-time resistive response of the sensor to a human pulse.

high-quality graphene. This method produces a flexible two-parameter sensor based on LIG, offering both remarkable sensitivity and stability. The sensor demonstrates an outstanding measurement factor of $4.16 \times 10^4$ and a rapid response time of 32 ms, making it highly capable of detecting subtle deformations of human skin. Furthermore, the sensor exhibits excellent temperature sensing capabilities, with a high sensitivity of 1.46%/°C within a detection range of 20 to 50 °C. This feature is crucial for developing electronic skin devices that require diverse sensing abilities. Using the efficiency of laser fabrication and the superior sensing performance of LIG sensors, producing LIG sensors based on PR holds immense promise for applications in human physiological health monitoring, electronic skin, wearable electronic devices, and beyond.

**Authors' contributions** M.G. and Z.Z. performed writing of the manuscript, designing of figures, and preparation of the initial draft of the manuscript; W.Z. and Y.G. reviewed and edited the manuscript; S.W. and X.L. provided valuable guidance. All authors have read and agreed to the final version of this manuscript.

**Declaration of competing interests** The authors declare that they have no competing interests relevant to the content of this article.

**Acknowledgements** This work was supported by the National Key Research and Development Program of China (Grant No. 2022YFB4600400) and the National Natural Science Foundation of China (Grant No. 52275401).

**Online appendix** Electronic supplementary material (ESM) can be found in the online version at https://doi.org/10.1007/s11706-024-0696-6 and https://journal.hep.com.cn/foms/EN/10.1007/s11706-024-0696-6 that includes Figs. S1–S6.

## References

[1] Ershad F, Thukral A, Yue J, et al. Ultra-conformal drawn-on-skin electronics for multifunctional motion artifact-free sensing and point-of-care treatment. Nature Communications, 2020, 11(1): 3823

[2] Mao L, Pan T, Lin L, et al. Simultaneously enhancing sensitivity and operation range of flexible pressure sensor by constructing a magnetic-guided microstructure in laser-induced graphene composite. Chemical Engineering Journal, 2024, 481: 148639

[3] Kim D S, Lee Y H, Kim J W, et al. A stretchable array of high-performance electrochromic devices for displaying skin-attached multi-sensor signals. Chemical Engineering Journal, 2022, 429: 132289

[4] Salvatore G A, Sülzle J, Dalla Valle F, et al. Biodegradable and highly deformable temperature sensors for the internet of things. Advanced Functional Materials, 2017, 27(35): 1702390

[5] Kim D H, Lu N, Ma R, et al. Epidermal electronics. Science, 2011, 333(6044): 838−843

[6] Lee G, Son J H, Lee S, et al. Fingerpad-inspired multimodal electronic skin for material discrimination and texture recognition. Advanced Science, 2021, 8(9): 2002606

[7] Yu R H, Wang C X, Du X H, et al. *In-situ* forming ultra-mechanically sensitive materials for high-sensitivity stretchable fiber strain sensors. National Science Review, 2024, 11(6): nwae158

[8] Avinash K, Patolsky F. Laser-induced graphene structures: from synthesis and applications to future prospects. Materials Today, 2023, 70: 104−136

[9] Yao S, Ren P, Song R, et al. Nanomaterial-enabled flexible and stretchable sensing systems: processing, integration, and applications. Advanced Materials, 2020, 32(15): 1902343

[10] Du Y, Zhang Q, Zhuo K, et al. Study on the performance of temperature-stabilised flexible strain sensors based on silver nanowires. Micro & Nano Letters, 2019, 14(2): 168−172

[11] Song R, Yao S, Liu Y, et al. Facile approach to fabricating stretchable organic transistors with laser-patterned Ag nanowire electrodes. ACS Applied Materials & Interfaces, 2020, 12(45): 50675−50683

[12] Miao Z Y, Yu R H, Bai X W, et al. Versatile graphene/polyelectrolyte aqueous dispersion for fiber-based wearable sensors and electroluminescent devices. Science China Materials, 2024, 67: 1915−1925

[13] Lynch P J, Ogilvie S P, Large M J, et al. Graphene-based printable conductors for cyclable strain sensors on elastomeric substrates. Carbon, 2020, 169: 25−31

[14] Li C, Yang S, Guo Y, et al. Flexible, multi-functional sensor based on all-carbon sensing medium with low coupling for ultrahigh-performance strain, temperature and humidity sensing. Chemical Engineering Journal, 2021, 426: 130364

[15] Huang H, Han L, Li J, et al. Super-stretchable, elastic and recoverable ionic conductive hydrogel for wireless wearable, stretchable sensor. Journal of Materials Chemistry A: Materials for Energy and Sustainability, 2020, 8(20): 10291−10300

[16] Dauzon E, Lin Y, Faber H, et al. Stretchable and transparent conductive PEDOT: PSS-based electrodes for organic photovoltaics and strain sensors applications. Advanced Functional Materials, 2020, 30(28): 2001251

[17] Lin J, Peng Z W, Liu Y Y, et al. Laser-induced porous graphene films from commercial polymers. Nature Communications, 2014, 5: 5714

[18] Kulyk B, Silva B F R, Carvalho A F, et al. Laser-induced graphene from paper for mechanical sensing. ACS Applied Materials & Interfaces, 2021, 13(8): 10210−10221

[19] Behrent A, Griesche C, Sippel P, et al. Process–property correlations in laser-induced graphene electrodes for electrochemical sensing. Mikrochimica Acta, 2021, 188: 159

[20] Zhu J, Liu S, Hu Z, et al. Laser-induced graphene non-enzymatic glucose sensors for on-body measurements. Biosensors & Bioelectronics, 2021, 193: 113606

[21] Li Y, Lei X, Guo D, et al. Laser-induced skin-like flexible pressure sensor for artificial intelligence speech recognition. ACS Applied Materials & Interfaces, 2024, 16(8): 10380−10388

[22] Thakur A K, Sengodu P, Jadhav A H, et al. Manganese carbonate/laser-induced graphene composite for glucose sensing. ACS Omega, 2024, 9(7): 7869−7880

[23] Liu H B, Xiang H C, Li Z J, et al. Flexible and degradable multimodal sensor fabricated by transferring laser-induced porous carbon on starch film. ACS Sustainable Chemistry & Engineering, 2020, 8(1): 527−533

[24] Le T S D, Park S, An J, et al. Ultrafast laser pulses enable one-step graphene patterning on woods and leaves for green electronics. Advanced Functional Materials, 2019, 29(33): 1902771

[25] Hong Q, Zhu W H, Wang S M, et al. High-resolution femtosecond laser-induced carbon and Ag hybrid structure for bend sensing. ACS Omega, 2022, 7(46): 42256−42263

[26] Bai R J, Gao Y, Lu C, et al. Femtosecond laser micro-fabricated flexible sensor arrays for simultaneous mechanical and thermal stimuli detection. Measurement, 2021, 169: 108348

[27] Zhu W H, Wang M M, Zhang Z, et al. Controllable photoreduction of graphene oxide/gold composite using a shaped femtosecond laser for multifunctional sensors. ACS Applied Materials & Interfaces, 2023, 15(45): 52883−52892

[28] Jiang S, Park C S, Lee W B, et al. Photoreduction-insensitive GO/rGO patterning based on multistep femtosecond laser writing for implementing Fresnel zone plates. ACS Applied Nano Materials, 2021, 4(9): 9283−9292

[29] Claro P I C, Pinheiro T, Silvestre S L, et al. Sustainable carbon sources for green laser-induced graphene: a perspective on fundamental principles, applications, and challenges. Applied Physics Reviews, 2022, 9(4): 041305

[30] Ferrari A C, Meyer J C, Scardaci V, et al. Raman spectrum of graphene and graphene layers. Physical Review Letters, 2006, 97(18): 187401

[31] Zhu J, Huang X, Song W. Physical and chemical sensors on the basis of laser-induced graphene: mechanisms, applications, and perspectives. ACS Nano, 2021, 15(12): 18708−18741

[32] Zhang X W, Pan Y, Zheng Q, et al. Time dependence of piezoresistance for the conductor-filled polymer composites. Journal of Polymer Science Part B: Polymer Physics, 2000, 38(21): 2739−2749

[33] Chhetry A, Sharifuzzaman M, Yoon H, et al. $MoS_2$-decorated laser-induced graphene for a highly sensitive, hysteresis-free, and reliable piezoresistive strain sensor. ACS Applied Materials & Interfaces, 2019, 11(25): 22531−22542

[34] Chen X, Luo F, Yuan M, et al. A dual-functional graphene-based self-alarm health-monitoring e-skin. Advanced Functional Materials, 2019, 29(51): 1904706

[35] Liu Y, Li H, Zhang M. Wireless battery-free broad-band sensor for wearable multiple physiological measurement. ACS Applied Electronic Materials, 2021, 3(4): 1681−1690

[36] Li Q, Wu T, Zhao W, et al. Laser-induced corrugated graphene films for integrated multimodal sensors. ACS Applied Materials & Interfaces, 2021, 13(31): 37433−37444

[37] Liu W, Chen Q, Huang Y, et al. *In situ* laser synthesis of Pt nanoparticles embedded in graphene films for wearable strain sensors with ultra-high sensitivity and stability. Carbon, 2022, 190: 245−254

[38] Liu W, Huang Y, Peng Y, et al. Stable wearable strain sensors on textiles by direct laser writing of graphene. ACS Applied Nano Materials, 2020, 3(1): 283−293

[39] Shirhatti V, Nuthalapati S, Kedambaimoole V, et al. Multifunctional graphene sensor ensemble as a smart biomonitoring fashion accessory. ACS Sensors, 2021, 6(12): 4325−4337

[40] Chhetry A, Sharma S, Barman S C, et al. Black phosphorus@laser-engraved graphene heterostructure-based temperature-strain hybridized sensor for electronic-skin applications. Advanced Functional Materials, 2021, 31(10): 2007661

[41] Chen X, Li R, Niu G, et al. Porous graphene foam composite-based dual-mode sensors for underwater temperature and subtle motion detection. Chemical Engineering Journal, 2022, 444: 136631